Supporting Information for

**Spatial and temporal evolution of earthquake dynamics: case study of the Mw 8.3 2015 Illapel Earthquake, Chile**

Jiuxun Yin[1], Marine A. Denolle[1], Huajian Yao[2]

1. Department of Earth and Planetary Sciences, Harvard University, Cambridge MA02138, USA

2. Laboratory of Seismology and Physics of Earth's Interior & School of Earth and Space Sciences, University of Science and Technology of China, Hefei, Anhui, 230026, China

**Contents of this file**

**Additional Supporting Information (Files uploaded separately)**

**Introduction**

In this supporting material, we present more figures to complement and support the main manuscript. Figure S1-S4 focus on our ImCS-BP methodology. Figure S5-S10 and Table S1 focus on the source spectral analysis.

In Figure S1, we show details about the data used in the ImCS-BP analysis. We use the seismic data recorded by the USArray (Figure S1 (a)-(b)) and all the seismic data downloadable from Wilber 3 of IRIS DMC, http://ds.iris.edu/wilber3/find_event). The raw data is first processed by removing the mean, trend, and instrumental responses. We then calculate the SNR for each trace (Hilbert transform of the event and noise time series and calculate the log amplitude ratio) and only keep the stations with SNR > 3 dB. Then the waveforms are filtered to low frequency band (LF: 0.08-0.5Hz) and high frequency band (HF: 0.5-1Hz) using a Butterworth bandpass filter. To suppress the effects of 3D structural heterogeneity, we apply a multichannel cross-correlation method [*VanDecar and Crosson*, 1990; *Ishii et al.*, 2007] for the first 8 seconds (solid lines in Figure S1, (c), (d) and zoom-ins in (e), (g)) to further align the waveforms relative to the P arrivals. The distributions of the final cross-correlation coefficients are shown in Figure S1 (f) and (h). We only keep the stations with cross-correlation coefficients greater than 0.8 for LF data and greater than 0.7 for HF data.

We also compare the computational efficiency for the CS-BP method with and without auto-adaptive refinements (Fig.S2). The setups of synthetic test are described in the main text and Figure 2. The source region is 360 km $\times$ 320 km and a uniform meshing with grid size of 5 km $\times$ 5 km, that is, 4745 unknown model parameters that are to be inverted. The CPU time for the set up with ideal but uniform resolution is about 120 seconds (red line in Figure S2). The improved CS-BP with auto-adaptive refinements is also tested. Because the refinement is iterative, we try 100 situations by randomly adding noise in the data (random phase and 10% of the maximum amplitude of input data). The CPU time is around 20 seconds for all cases, much less than the uniform meshing because of the smaller model space. This technique has the potential to obtain higher spatial resolution around the position of the sources for earthquakes with extremely large area, such as the 2004 Sumatra earthquake, or in the case of continuous global backprojection for earthquake detection.

As for the possible complexity of the large earthquake and to test the resolution of our methods, we also design a synthetic test representing a more complicated rupture process in Figure S3. The synthetic sources are more closely located so the generated synthetic waveforms suffer more severely from overlapping and interfering. Moreover,

two unilateral scenarios are used to construct a bilateral but generally unilateral rupture process. In the low frequency band [0.08 0.5] Hz, the general process can be recovered but due to the spatial resolution, our back-projection method cannot resolve the two scenarios. On the other hand, for the high frequency band [0.5 1] Hz, once the synthetic sources propagate far enough, our method can resolve these two scenarios.

In Figure S4, we show the example of the apparent shift effect on the truncated time window and the time adjustments for the real event data (80 s, 90 s, 100 s, 110 s, and 120 s). The first row presents the uncorrected waveforms (CS-BP results) in Figure 5 (a). The truncation effects (defined in main manuscript) are very clear for these time windows and have brought some scatters to the locations of the coherent bursts in Figure 5 (a). However, after the time-adjustment, the waveforms in each time window become more coherent (second row in Figure S4), stabilizes the results with less blurring between the bursts (Fig.5 (b)).

Figure S5 and S6 show the station and SNR distributions for each EGF event chosen in the source spectral analysis, respectively. The distribution of the stations is quite non-uniform in azimuth: while there is almost no station within 200˚-320˚, there are denser stations within 320˚-0˚ (USArray). Therefore, in the stacking process, we weighted the spectra by the number of the stations within each azimuth bin. After selecting data for quality, we use a total of 1811 waveforms.

Figure S7 presents the reconstructed source spectrum as well as the best fitted source model of the Mw 8.3 main event within 0.08-2 Hz in each 10˚ azimuth bin. Figure S8 indicates the fitted and calculated source parameters (radiated energy, $f_c$, falloff rate, $f_{c1}$ and $f_{c2}$) for each station as well as their median. While there are some azimuthal variations of these parameters, the pattern is not clear and we propose that it is due to the limitation of simple source model.

In order to relate canonical slip rate function shapes and spectral falloff rate, we take various kinds of slip rate functions listed in *Tinti et al.* [2005], compute their Fourier transform, and compare their spectral falloff rates (Figure S9). There are very clear differences and we propose that our observations on the time-varying falloff rate may reflect the variation of slip rate function shapes within the corresponding time window.

Figure S10 shows preliminary results on synthetic source spectrogram analysis. We construct a pure thrust event of source dimension 60 km × 100 km with a 30 degrees dip, a seismic moment of $3 \times 10^{20}$ Nm (translate that into moment magnitude). We use the kinematic source generator [*Schmedes et al.*, 2010; *Crempien and Archuleta*, 2014] to create a distribution of slip, rise times, and onset time. We use the dynamically

self-consistent regularized Yoffe function [*Tinti et al.*, 2005] at each pixel of the kinematic sources, with an asymmetry of 30% in each slip rate functions. We construct far-field synthetic P waves and perform the source spectrogram analysis as described in the main manuscript. We show in (a) the normalized source time function (proportional to slip-rate function) and the source time function (STF) filtered at high frequencies (0.2 Hz to 9 Hz); (b) the evolution of the radiated energy; (c) high-frequency falloff rate *n*, and (d) the Fourier amplitude source spectrogram.

In Table S1, we show the effects from attenuation *t\** model on the source parameters of EGF events. The *t\** model is used by multiplying the spectrum of Green's function produced in equation (6) by $\exp\left(-\pi f t^*\right)$. We test two global *t\** model: The first one is from *Warren and Shearer* [2000], a global average *t\** model and *t\** is a simple function of source-station distance and frequency. The second model is from *Warren and Shearer* [2002], a laterally heterogeneous *t\** model and we account for regional perturbations both at the source and at the receiver, $t^{*\prime} = t^* + dt^*_{source} + dt^*_{receiver}$. The best fit source parameters using these two attenuation models are similar (almost the same corner frequency and a slightly larger falloff rate *n* from the second model) as listed in Table S1. Therefore, in the main text we use the first model for simplicity.

The Supplement S1 file shows (a) the details of EGF source spectrum fitting including all the recovered spectra (blue lines), best-fitting spectral line from Aki type model (*Aki* [1967] and equation (7) in the main text or in *Brune* [1970, 1971]) allowing for a variable falloff rate *n* (red solid line with circle), the double-corner frequency model (red dotted line with squares) proposed by *Denolle and Shearer* [2016] (equation (14) in the main text), and compared with a model for which we assume a 3 MPa stress drop model (with a uniform stress drop on a circular patch [*Eshelby*, 1957; *Brune*, 1970, 1971]). (b) source depth correction with dashed line indicating the GCMT centroid depth and yellow circle indicating the corrected source depth. (c) Fitting residual distribution. Solid white line shows the region within the residual contour of 0.1 and we use the model parameters within this region to estimate the spectral uncertainty. (d) Bold black line is the stacked source spectrum and red line with circle is the optimal spectral model same as (a). Thinner gray lines are the spectral models with fitting residual less than 0.1 (within the white solid line in (c)). We take the region illustrated by these models (yellow shadow region with brown outline) to represent the source spectral uncertainty and to estimate the uncertainty of the main event.

The Supplement movie S1 show the time-varying spectral analysis results, including the recovered source spectra, corresponding uncertainties from the eGf source spectra, and the best-fitting straight lines to get falloff rate in the LF and HF frequency bands.
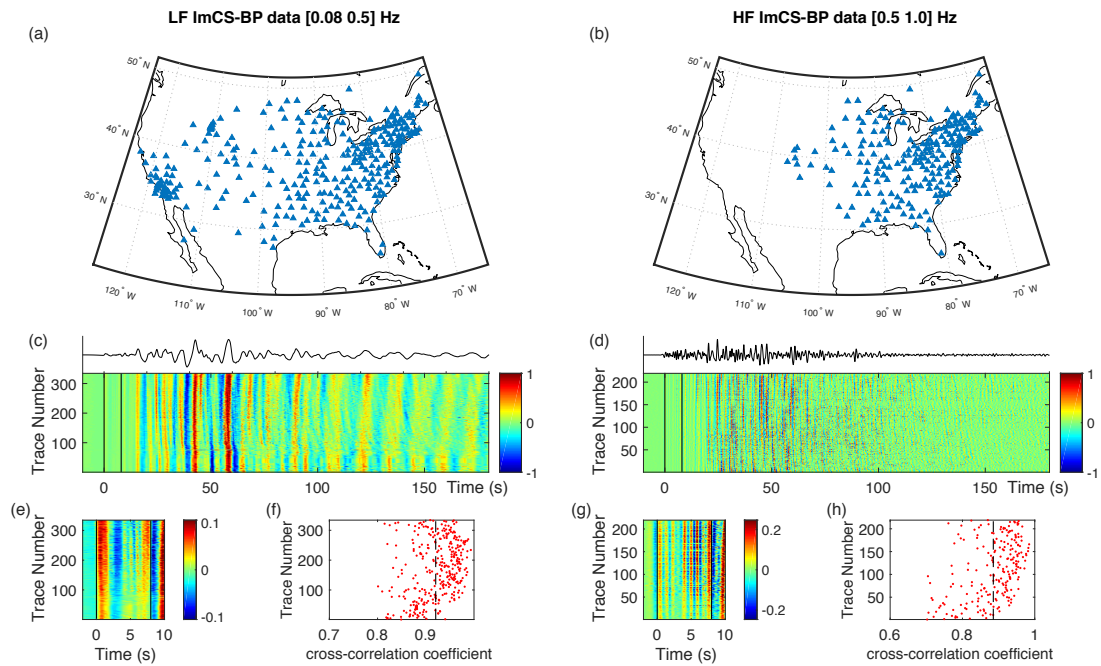
Figure S1. Data processing for the ImCS-BP. We used the data recorded by the US array stations in North America (TA array shown in the maps (a) and (b), data available at the Incorporated Research Institutions for Seismology Data Management Center, IRIS-DMC). The aligned waveform data is shown in (c) and (d), the top waveforms are the stacked waveforms for comparison. Two solid lines in both (c) and (d) indicate the window within which the waveforms are used to do the cross-correlation. (e) – (h) show the zoom-ins of these cross-correlation windows as well as the final cross-correlation coefficients distribution. Dashed lines are the average cross-correlation coefficients.
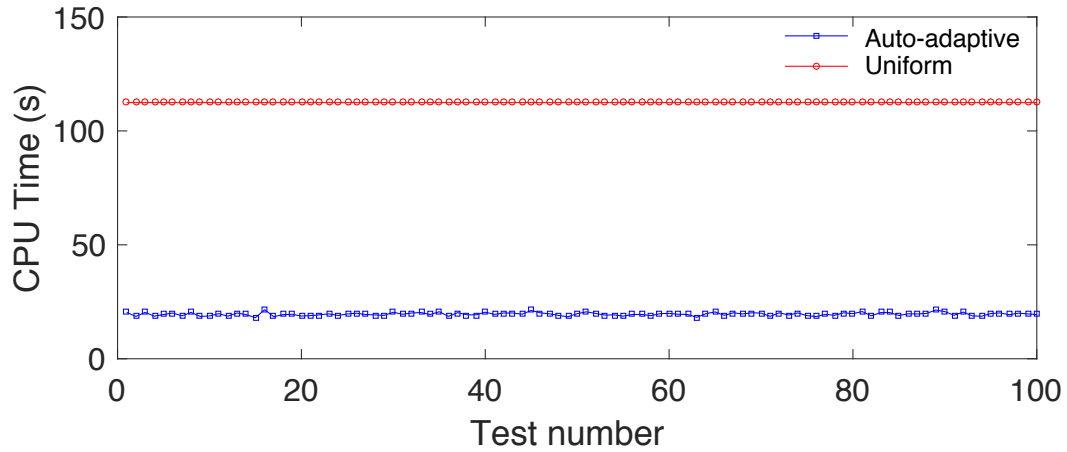
Figure S2. Computational efficiency for the ImCS-BP method. We run the synthetic test mentioned in Section 2.1 (Fig.2) on a laptop with 2.9 GHz Intel Core i5 processor for 100 times with different random noises (10% of maximum amplitude of the input data, random phase) added to the input data. Red circles show the CPU time for conventional CS-BP method with uniform grid (grid size of 5 km, totally 4745 grid points) while the blue squares show the CPU time for the ImCS-BP method with auto-adaptive grid size.
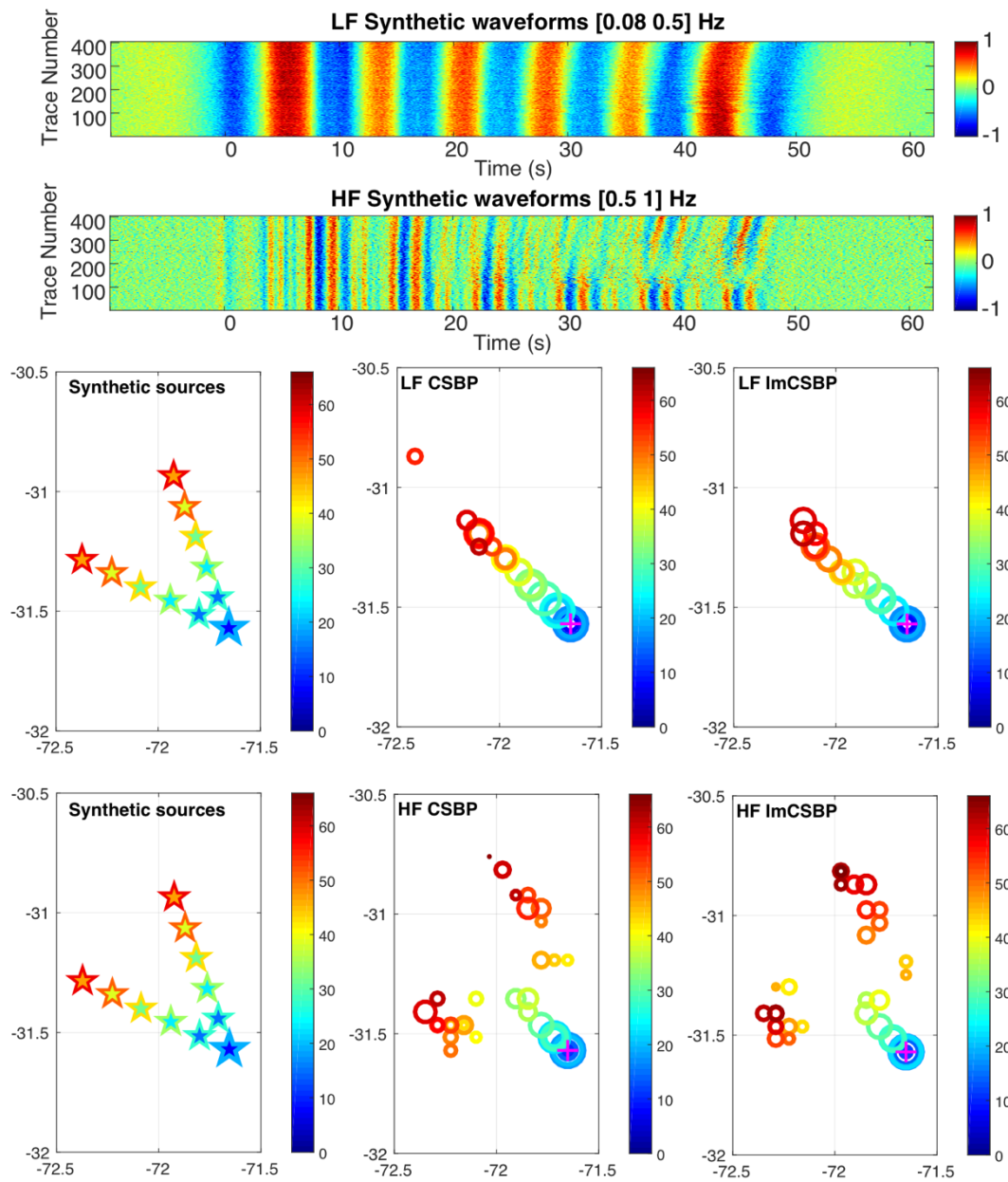
Figure S3. Results of a more complex synthetic test. Stars indicate the synthetic sources and their color show the source time. The face and edge color present the starting and ending time of these synthetic sources, respectively. The corresponding synthetic waveforms that are produced using the same method mentioned in the main text is shown by the top two panels. Colored circles indicate the recovered results by our different backprojection methods, whose name is labelled on the top left in each panel.
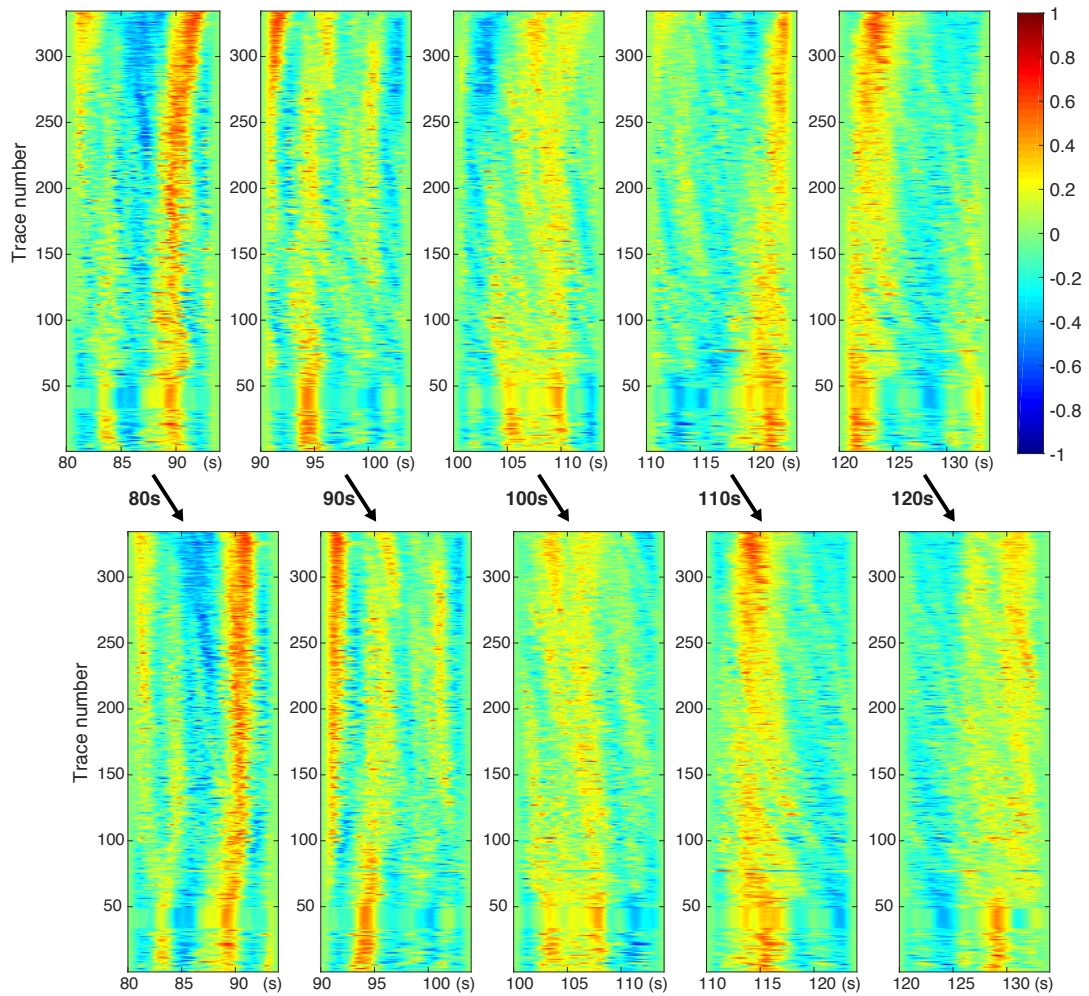
Figure S4. Examples for the waveform truncation of the real seismic data of the 2015 Illapel, Chile event. The first row shows the data without the sliding time window adjustment. The second row shows the data after time adjustment for the same time window.
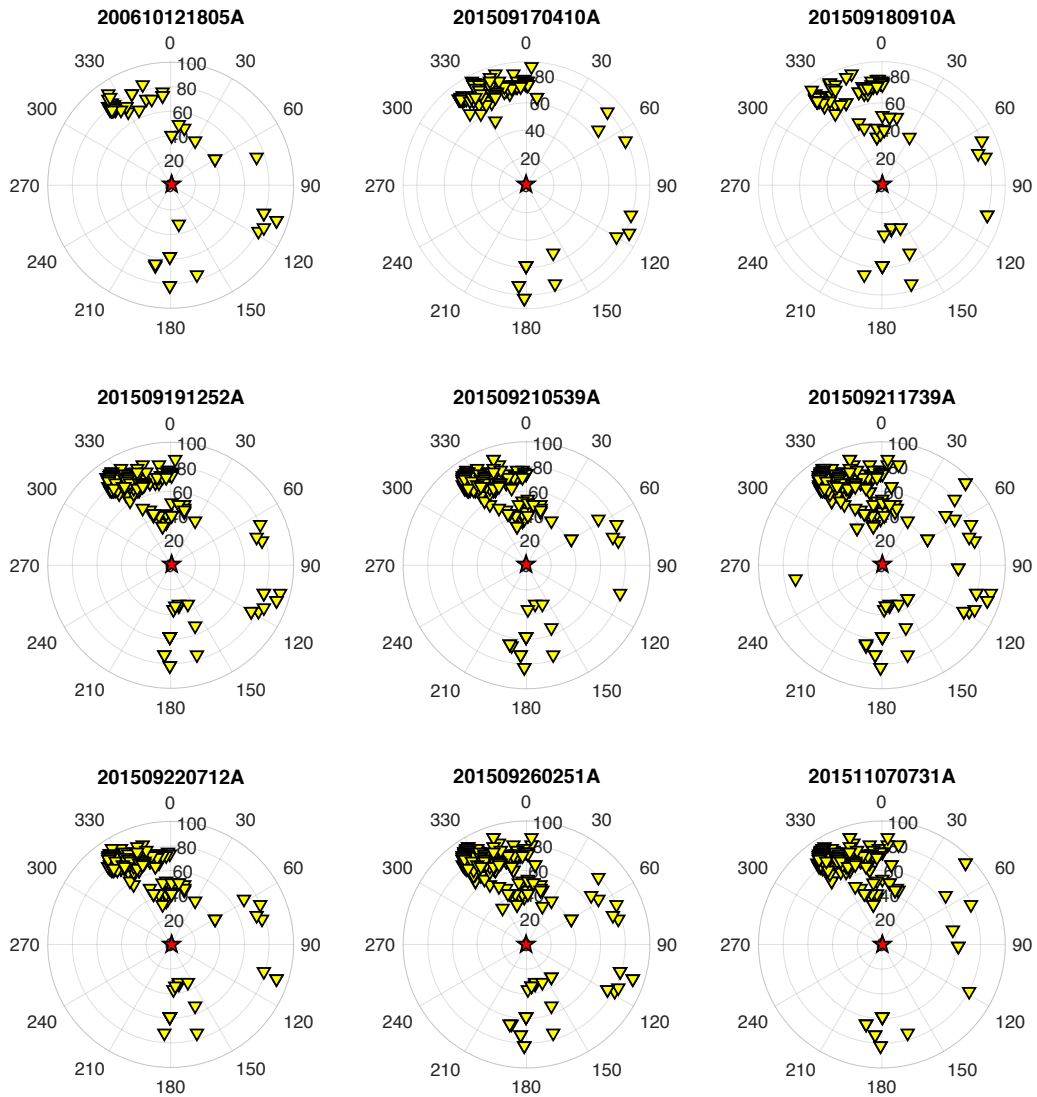
Figure S5. Station (yellow triangles) distributions (with azimuth and great circle distance) for each EGF event used in the source spectral analysis. Red stars show the location of Mw 8.3 main epicenter with respect to the stations.
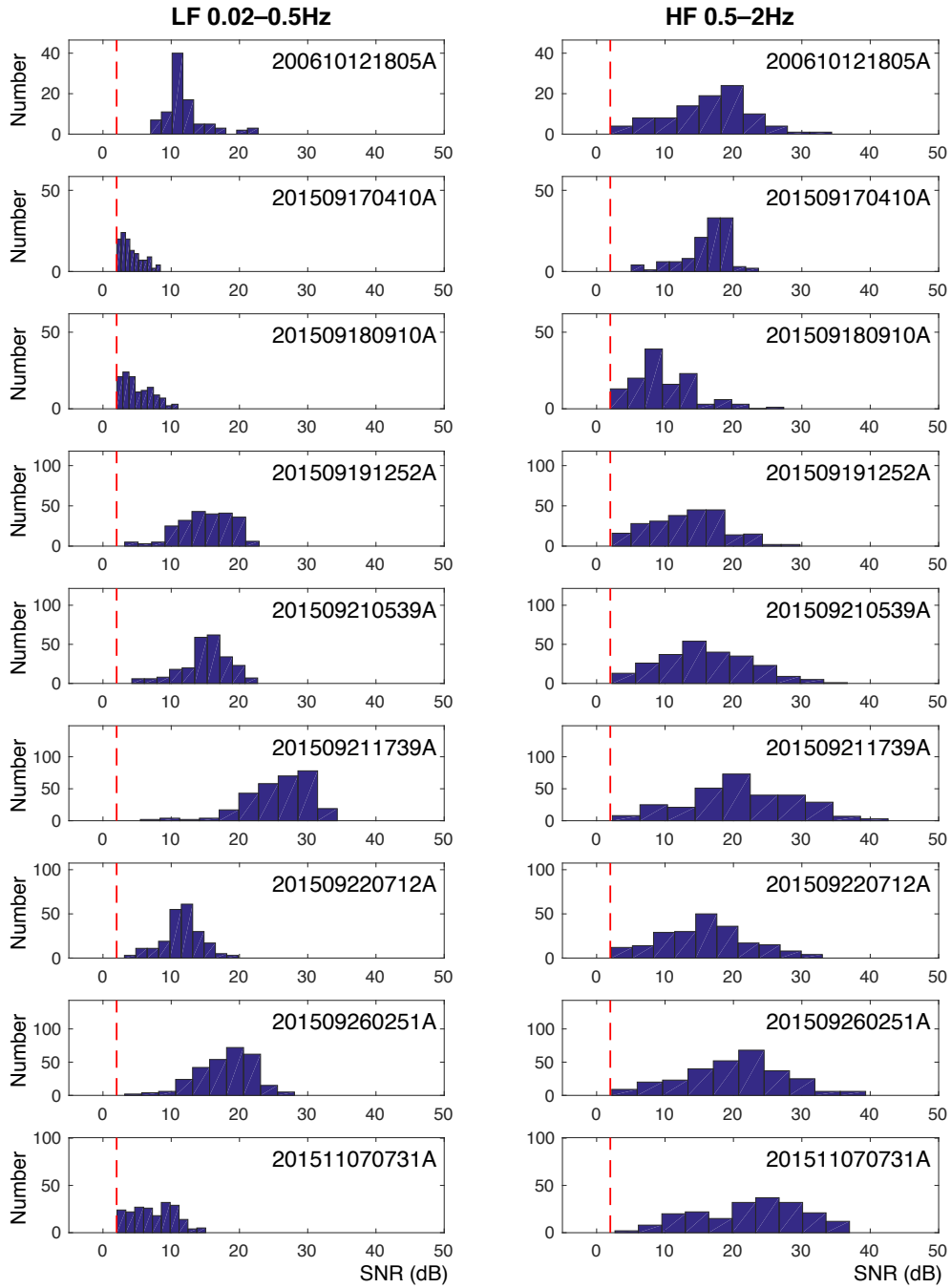
Figure S6. SNR distributions of our data for the spectral analysis. Red dashed lines indicate our SNR criterion of 2 dB. SNRs are estimated for each station and each event in low frequency (LF) and high frequency (HF) bands, respectively.
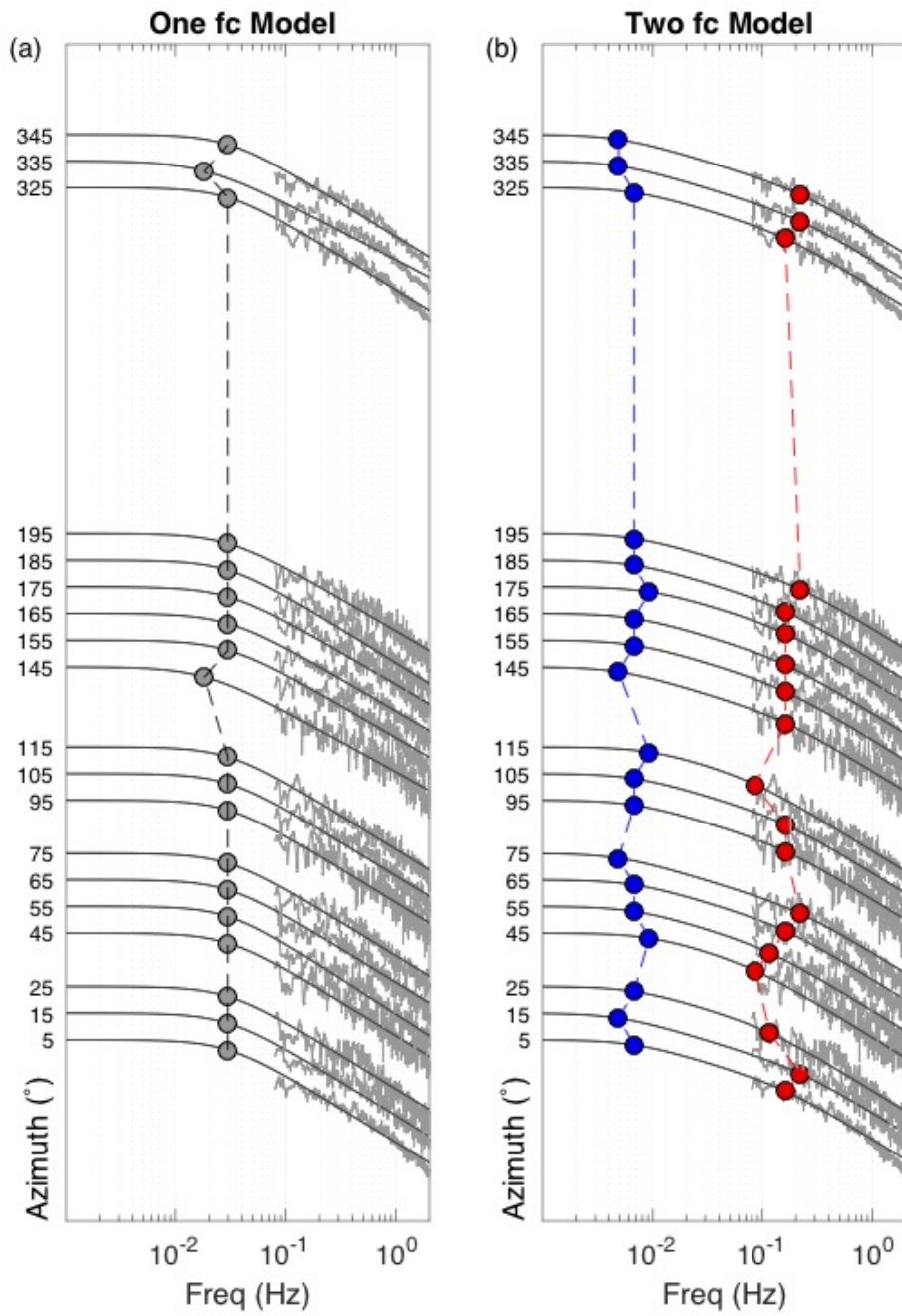
Figure S7. Spectral fitting for the total event source spectrum in each azimuth bin using single corner frequency model (a) as well as double corner frequency model (b). Circles indicate the best-fitting corner frequency of each spectrum line.
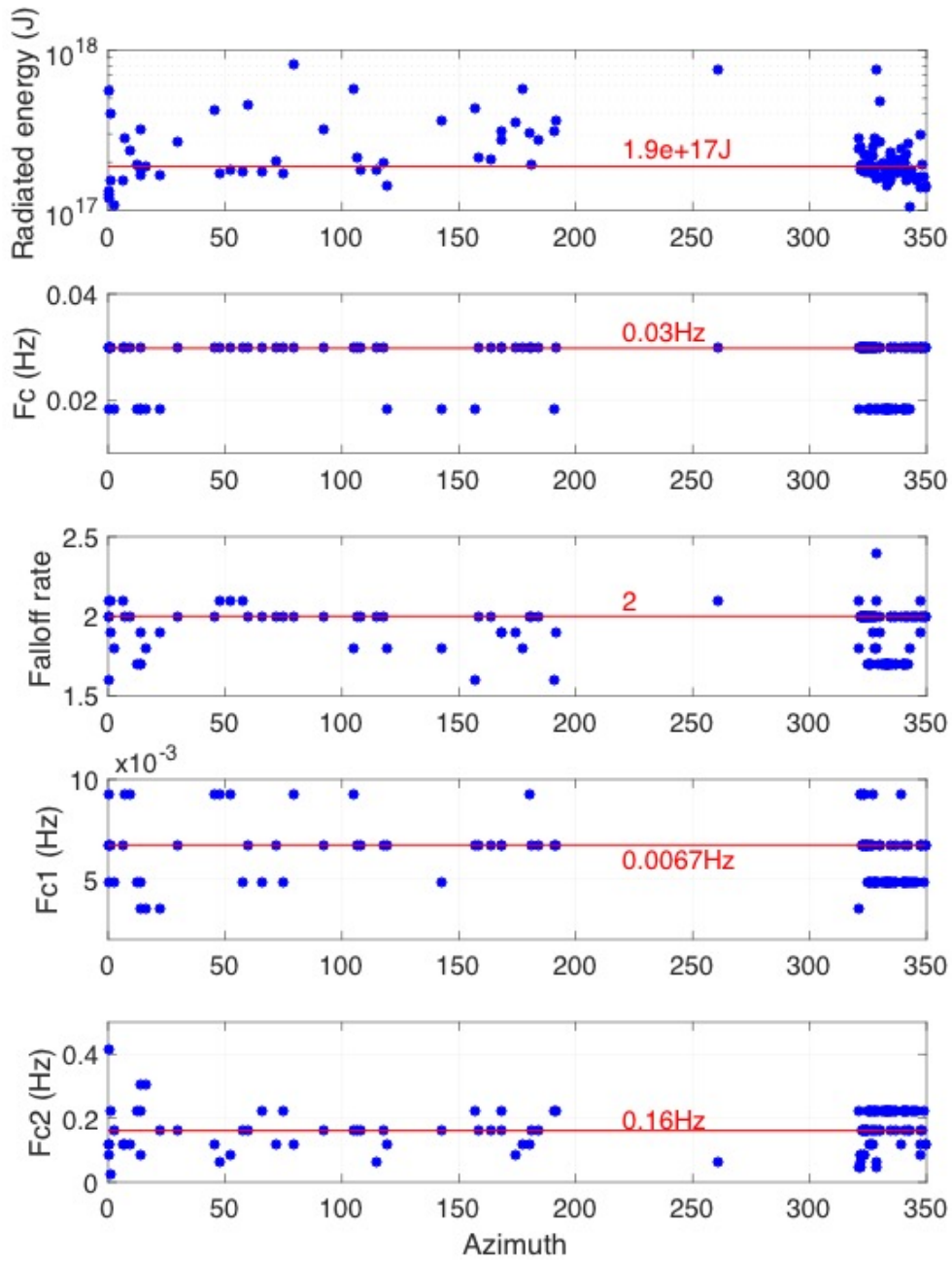
Figure S8. Source parameters estimated from the source spectrum at each station. Red lines show the median value for all the measurements. Radiated energy is calculated based on equations (12) – (13) in the main manuscript. Fc and falloff rate are from the single-corner frequency model (equation (7) in the main manuscript) fitting. Fc1 and Fc2 are the two corner frequencies from the double corner frequency model (equation (14) in the main manuscript) fitting.
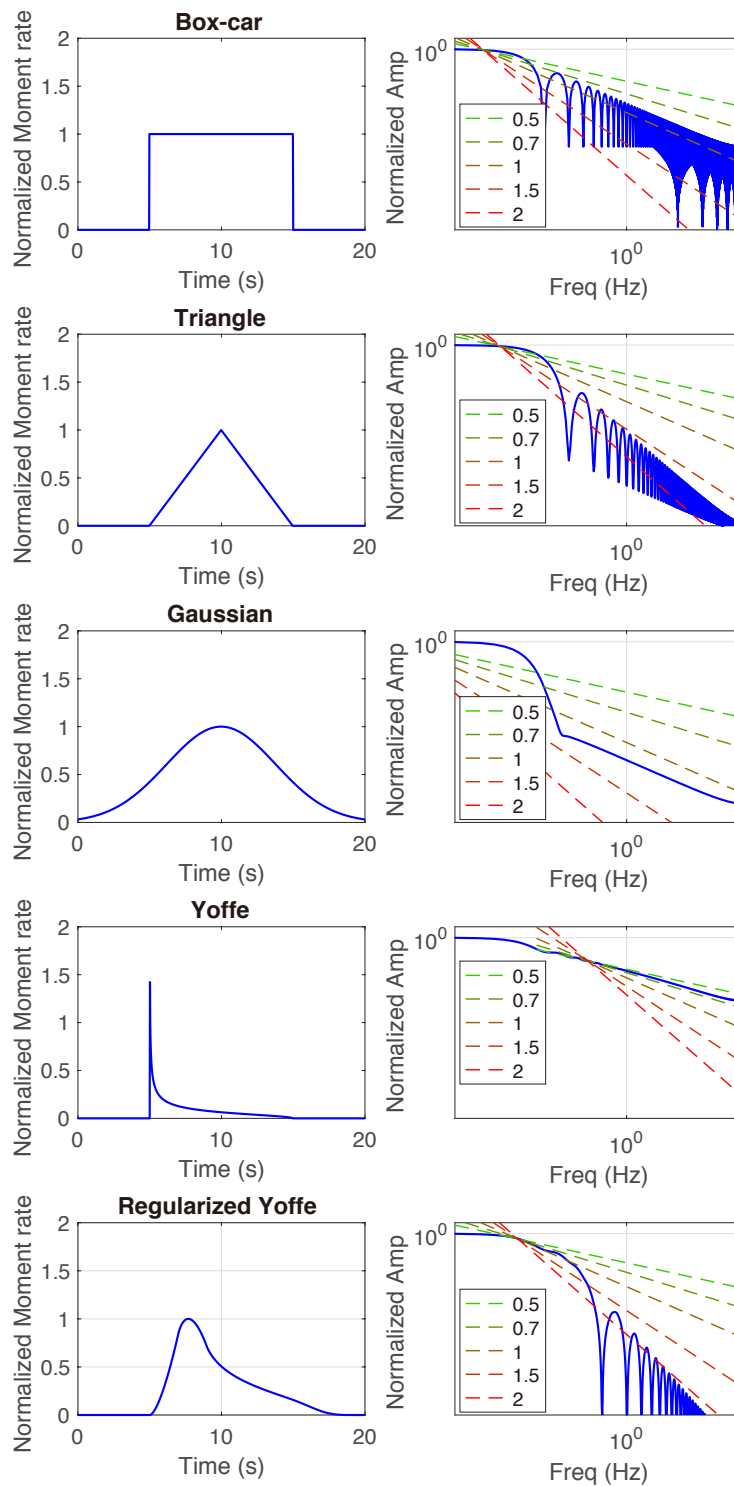
Figure S9. Various canonical slip rate function shapes mentioned in *Tinti et al.* [2005] are shown in the left column. The corresponding amplitude spectrum of each slip rate function is shown on the right. Colored dashed lines are the references for different values of falloff rate.
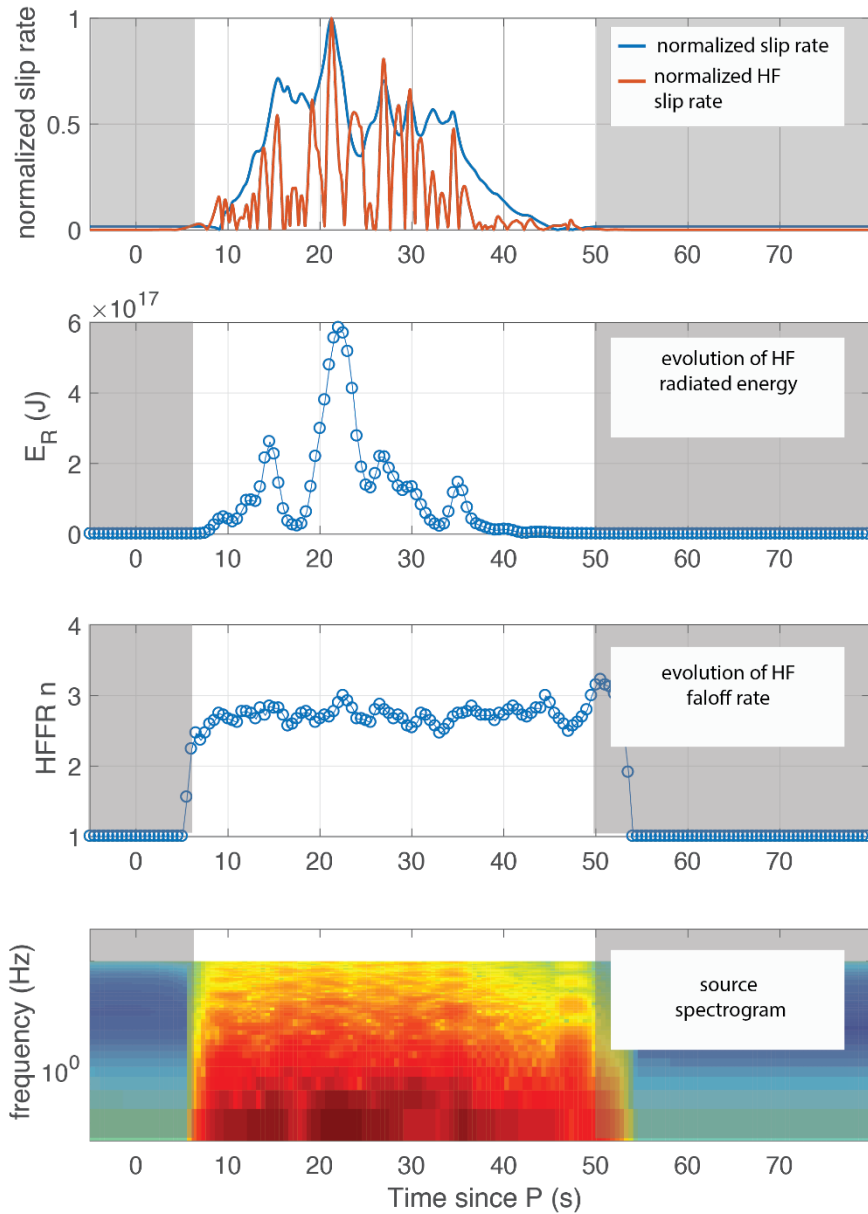
Figure S10. Preliminary results of the source spectral analysis on the synthetic kinematic source: (a) the normalized source time function (proportional to slip-rate function, blue line) and the STF filtered at high frequencies (0.2 Hz to 9 Hz, red line); (b) the evolution of the radiated energy; (c) high-frequency falloff rate $n$, and (d) the Fourier amplitude source spectrogram.

| Event (GCMT ID) | $t^*$ | | $t^* + dt^*$ | |
|---|---|---|---|---|
| | $f_c$ | $n$ | $f_c$ | $n$ |
| 200610121805A | 0.33 | 2.8 | 0.33 | 3.0 |
| 201509170410A | 0.13 | 2.2 | 0.17 | 2.6 |
| 201509180910A | 0.33 | 2.8 | 0.33 | 3.2 |
| 201509191252A | 0.33 | 2.8 | 0.33 | 2.8 |
| 201509210539A | 0.45 | 3.0 | 0.45 | 3.2 |
| 201509211739A | 0.33 | 3.0 | 0.33 | 3.2 |
| 201509220712A | 0.62 | 3.2 | 0.62 | 3.4 |
| 201509260251A | 0.45 | 3.0 | 0.45 | 3.4 |
| 201511070731A | 0.33 | 3.0 | 0.33 | 3.2 |

Table S1. Comparison between source parameters (corner frequency and high frequency falloff rate) of EGF source models using global $t^*$ attenuation model [*Warren and Shearer*, 2000] as well as spatially variable attenuation model $t^* + dt^*$ [*Warren and Shearer*, 2002].

**References:**

Aki, K. (1967), Scaling law of seismic spectrum, *J. Geophys. Res.*, *72*(4), 1217–1231, doi:10.1029/JZ072i004p01217.

Brune, J. N. (1970), Tectonic stress and the spectra of seismic shear waves from earthquakes, *J. Geophys. Res.*, *75*(26), 4997–5009, doi:10.1029/JB075i026p04997.

Brune, J. N. (1971), Correction (to Brune, 1970), *J Geophys Res*, *76*, 5002.

Crempien, J. G. F., and R. J. Archuleta (2014), UCSB Method for Simulation of Broadband Ground Motion from Kinematic Earthquake Sources, *Seismol. Res. Lett.*, doi:10.1785/0220140103.

Denolle, M. A., and P. M. Shearer (2016), New perspectives on self-similarity for shallow thrust earthquakes, *J. Geophys. Res. Solid Earth*, *121*(9), 2016JB013105, doi:10.1002/2016JB013105.

Eshelby, J. D. (1957), The determination of the elastic field of an ellipsoidal inclusion, and related problems, in *Proceedings of the Royal Society of London A: Mathematical, Physical and Engineering Sciences*, vol. 241, pp. 376–396, The Royal Society.

Ishii, M., P. M. Shearer, H. Houston, and J. E. Vidale (2007), Teleseismic P wave imaging of the 26 December 2004 Sumatra-Andaman and 28 March 2005 Sumatra earthquake ruptures using the Hi-net array, *J. Geophys. Res. Solid Earth*, *112*(B11), B11307, doi:10.1029/2006JB004700.

Schmedes, J., R. J. Archuleta, and D. Lavallée (2010), Correlation of earthquake source parameters inferred from dynamic rupture simulations, *J. Geophys. Res. Solid Earth*, *115*(B3), B03304, doi:10.1029/2009JB006689.

Tinti, E., E. Fukuyama, A. Piatanesi, and M. Cocco (2005), A Kinematic Source-Time Function Compatible with Earthquake Dynamics, *Bull. Seismol. Soc. Am.*, *95*(4), 1211–1223, doi:10.1785/0120040177.

VanDecar, J. C., and R. S. Crosson (1990), Determination of teleseismic relative phase arrival times using multi-channel cross-correlation and least squares, *Bull. Seismol. Soc. Am.*, *80*(1), 150–169.

Warren, L. M., and P. M. Shearer (2000), Investigating the frequency dependence of mantle Q by stacking P and PP spectra, *J. Geophys. Res. Solid Earth*, *105*(B11), 25391–25402, doi:10.1029/2000JB900283.

Warren, L. M., and P. M. Shearer (2002), Mapping lateral variations in upper mantle attenuation by stacking P and PP spectra, *J. Geophys. Res. Solid Earth*, *107*(B12), 2342, doi:10.1029/2001JB001195.